International Journal of Solids and Structures 102–103 (2016) 66–76

Contents lists available at ScienceDirect

International Journal of Solids and Structures

journal homepage: www.elsevier.com/locate/ijsolstr

A double-Westergaard model for adhesive contact of a wavy surface

Fan Jin[a], Qiang Wan[a], Xu Guo[b,*]

[a] Institute of Systems Engineering, China Academy of Engineering Physics, Mianyang, Sichuan 621900, PR China
[b] State Key Laboratory of Structural Analysis for Industrial Equipment, Department of Engineering Mechanics, International Research Center for Computational Mechanics, Dalian University of Technology, Dalian, 116023, PR China

ARTICLE INFO

Article history:
Received 9 July 2016
Revised 11 September 2016
Available online 19 October 2016

Keywords:
Contact mechanics
Adhesion
Wavy surface
Double-Hertz model
Adhesion hysteresis

ABSTRACT

This paper extends the double-Hertz model of Greenwood and Johnson (1998) to the plane strain problem of adhesive contact between a wavy surface and a flat surface, named as the double-Westergaard model. The adhesive force within the cohesive zone near contact edge is described by the difference between two Westergaard pressure distribution functions with different contact widths. Closed-form analytical solutions are obtained for different equilibrium states during loading and unloading stages. The proposed model captures a transition between Westergaard and JKR contact models through a dimensionless transition parameter. Depending on two dimensionless parameters, transitions between partial and full contact during loading/unloading are characterized by one or more jump instabilities. Decreasing waviness size by decreasing both the amplitude and period with a fixed curvature is found to enhance adhesion both by increasing the magnitude of the pull-off force and by inducing more energy loss through adhesion hysteresis.

1. Introduction

Recent developments in micro-fabrication techniques have led to a variety of methods to create well-defined surfaces at smaller and smaller scales with more and more controlled topographical features (Etsion, 2005). Compared with a smooth surface, surfaces with controlled topography are often favored in such applications as mechanical seals (Etsion and Halperin, 2002), microelectromechanical systems (MEMS) (Komvopoulos, 2003) and biomimetic designs (Hui et al., 2004). As the characteristic length scale of devices is reduced to micro- and nano-scales, interfacial adhesion becomes more prevalent as a result of molecular forces. These developments are calling for theoretical models that can be used to guide the design of topographical surfaces with controlled adhesion.

The effects of surface roughness on adhesion have been of interest for several decades. Experiments performed by Fuller and Roberts (1981) and later by Kim and Russell (2001) demonstrated that, with rising surface roughness, the adhesion increases initially and then decreases beyond certain threshold. The common sense of poor adhesion between stiff materials has been explained by a number of random multi-asperity contact models based on the classical Greenwood–Williamson theory, including JKR (Fuller and Tabor, 1975), Maugis–Dugdale (Morrow et al., 2003) and double-Hertz types (Zhang et al., 2014) of rough surface adhesion models. In these studies, a rough surface was considered as an ensemble of non-interacting asperities with height following a Gaussian distribution and with contact behavior of each individual asperity obeying a chosen model in adhesive contact mechanics. In this approach, multi-asperity roughness was found to induce adhesion hysteresis in different loading/unloading paths, resulting in an irreversible energy loss (Wei et al., 2010; Zhang et al., 2014). Due to the inherent assumption of negligible interaction between asperities, these models are only applicable for surfaces with sufficiently large roughness.

For surfaces with relatively small roughness, on the other hand, the interaction between asperities is expected to play an important to dominant role in determining the interaction between two contacting surfaces, which is known to result in roughness enhanced adhesion (Briggs and Briscoe, 1977; Santos et al., 2005). A one-dimensional sinusoidal wavy surface is one of the simplest models of periodic and continuous surface roughness, which lends itself to exact analytical solutions and has been employed in several previous studies (Johnson, 1995; Hui et al., 2001). For an axisymmetric wavy surface in contact with a spherical indenter, a JKR-type model was established by Guduru (2007), who found surface waviness tends to render the detachment process oscillatory with intrinsic instabilities, leading to a higher pull-off force and interfacial toughening through irreversible energy loss. Based on Guduru's solution, Kesari and Lew (2011) revealed an increase in energy loss due to adhesion hysteresis associated with surface waviness. Similar conclusion was also proposed for power-law graded elastic

* Corresponding author. Fax: +8641184707807.
E-mail address: guoxu@dlut.edu.cn (X. Guo).

http://dx.doi.org/10.1016/j.ijsolstr.2016.10.016
0020-7683/

solids with small (Jin and Guo, 2013) and large (Jin et al., 2016) surface roughness. Jin et al. (2011) carried out a systematic experimental study on a rippled surface with varying amplitudes, and reported different transition behaviors from partial to full contact depending on the waviness-amplitude.

For the plane strain problem of wavy surface adhesion, Johnson (1995) developed a JKR-type model for a sinusoidal wavy surface, combining the non-adhesive contact solution of Westergaard (1939) with that of an array of collinear cracks, and determined a critical value of the contact pressure for the wavy surface to come into full contact with a flat surface. Hui et al. (2001) extended this model to a Maugis–Dugdale type adhesion, so that the adhesive forces are no longer confined to a small region near the edge of the contact zone. They also derived a closed-form analytical solution but ignored the case of adhesion force acting along the whole interface. A similar Maugis–Dugdale type analysis of a wavy surface was also performed using potential functions by Adams (2004) who, based on three possible types of solutions, showed that the applied pressure versus contact size curves are characterized by discontinuities and hysteresis with jump instabilities during loading/unloading. Recently, this problem was reconsidered by Wu (2012) using a self-consistent numerical simulation based on the Lennard–Jones potential, which can cover the whole range of adhesive contact behaviors ranging from JKR to rigid contact. A transition between partial and full contact was demonstrated also for other periodic surfaces, including a sinusoidal wavy surface in symmetric (Zilberman and Persson, 2002) and non-symmetric (Carbone and Mangialardi, 2004) forms, as well as a periodic grooved surface (Chumak, 2016).

The classical adhesive contact theories for single spheres laid a solid foundation for the study of adhesion on wavy surfaces. In parallel with the Maugis–Dugdale model, Greenwood and Johnson (1998) proposed an alternative cohesive zone model, known as the double-Hertz model, which is applicable to arbitrary values of Tabor's parameter (Tabor, 1977). In this model, the adhesive force within the cohesive zone is described by the difference between two Hertzian pressure distribution functions with different contact radii. It was found that results obtained from the double-Hertz model are very close to those from the Maugis–Dugdale model, while the double-Hertz model is analytically more tractable than the Maugis–Dugdale model since the corresponding analysis relies solely on the classical Hertzian solutions. For this reason, the double-Hertz model is often adopted to study adhesion of complex contact systems involving rough contact surfaces (Zhang et al., 2014), cylindrical contact (Jin et al., 2014), viscoelastic materials (Haiat et al., 2003) and functionally graded elastic solids (Jin et al., 2013).

The present study is aimed to extend the double-Hertz model to the plane strain adhesive contact problem of a wavy surface, named as the double-Westergaard model, with emphasis on establishing a set of analytical solutions which are applicable for a full range of Tabor parameters. These solutions are analogous to the Maugis–Dugdale model and capable of describing a full range of behaviors from Westergaard to JKR, as well as different transitions between partial and full contact during loading/unloading. The rest of the paper is organized as follows. Section 2 establishes the analytical model for a wavy surface. Section 3 shows that both Westergaard and JKR solutions can be recovered as limiting cases associated with a dimensionless transition parameter. Based on these results, various loading/unloading curves and critical forces are examined in Sections 4, and 5 concludes the study.

2. The model

Fig. 1 shows the plane strain problem of adhesive contact between two dissimilar elastic bodies, one of which is flat and the other has a wavy profile with a small waviness amplitude. The contact bodies have Young's moduli E_1, E_2 and Poisson's ratios ν_1, ν_2, and are pressed together by a uniform remote traction $\bar{p}$ (negative when tensile), resulting in a contact half-width a within each period. Prior to loading, the surface of the upper body has a sinusoidal profile with amplitude Δ and wavelength L in the form

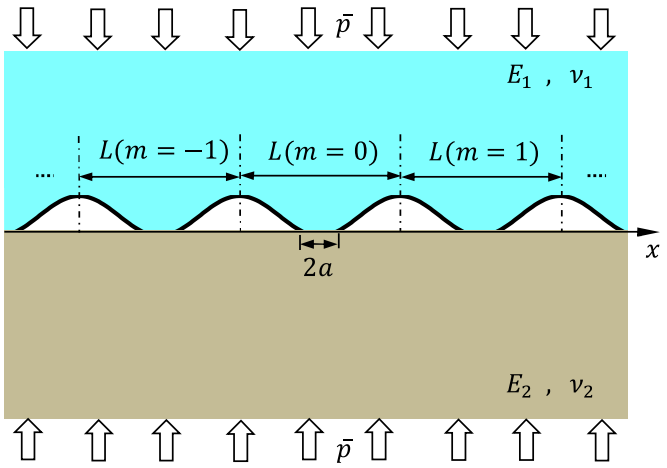

Fig. 1. Schematics of adhesive contact between an elastic flat surface and an elastic wavy surface with period L subjected to a remotely applied traction $\bar{p}$ (negative when tensile).

$$f(x)=\Delta\left(1-\cos\left(\frac{2\pi x}{L}\right)\right)=2\Delta\sin^2\left(\frac{\pi x}{L}\right) \tag{2.1a}$$

the curvature at a wave crest being

$$\frac{1}{R}=\frac{4\pi^2\Delta}{L^2} \tag{2.1b}$$

Alternatively, the wavy surface can be expressed in terms of R as

$$f(x)=\frac{L^2}{2\pi^2 R}\sin^2\left(\frac{\pi x}{L}\right) \tag{2.1c}$$

Note that for small x,

$$f(x)\approx\frac{x^2}{2R} \tag{2.1d}$$

which is the usual parabolic approximation for a cylinder of radius R.

Within each period (Fig. 2), the distribution of surface traction consists of two terms: the Westergaard pressure p_W acting on a contact region of width $2a$ and the adhesive tension p_A acting on an interaction zone of width $2c$. The noncontact regions $a\le|x|\le c$, $z=0$ are known as the cohesive zones.

The relative normal surface displacement $u_z(x)$ can be related to the surface traction $p(x)$ through surface Green's function as (Hui et al., 2001; Block and Keer, 2008):

$$-\frac{\partial u_z(x)}{\partial x}=\frac{\mathrm{d}f(x)}{\mathrm{d}x}=\frac{2}{\pi E^*}\sum_{m=-\infty}^{\infty}\int_{mL-a}^{mL+a}\frac{p(s)}{x-s}\mathrm{d}s$$
$$=\frac{2}{E^*L}\int_{-a}^{a}p(t)\cot\left(\frac{x-t}{L}\pi\right)\mathrm{d}t \tag{2.2a}$$

where

$$1/E^*=\left(1-\nu_1^2\right)/E_1+\left(1-\nu_2^2\right)/E_2 \tag{2.2b}$$

2.1. Westergaard solution

In the absence of adhesive interactions, the corresponding Hertz type contact solution for a sinusoidal wavy surface, known as the

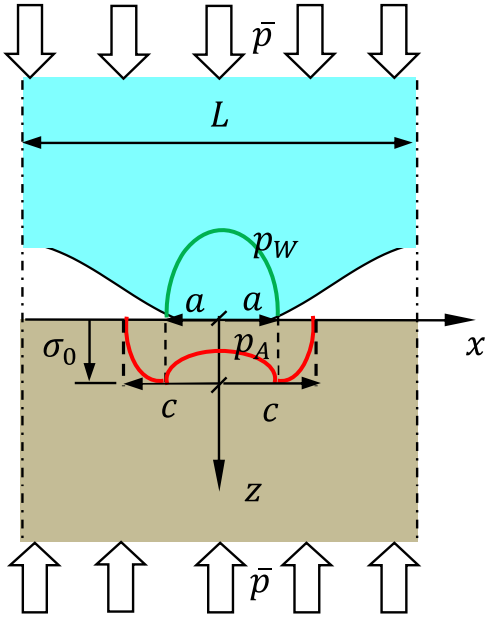

Fig. 2. Adhesive contact of a periodic wavy surface within one period. The distribution of surface traction consists of two terms: the Westergaard pressure p_W acting on the contact zone of width $2a$ and an adhesive traction p_A acting on the interaction zone of width $2c$.

Westergaard solution (Westergaard, 1939; Johnson, 1985), gives the contact pressure distribution as

$$p(x) = \frac{E^*L}{2\pi R}\cos\psi\sqrt{\sin^2\psi_a - \sin^2\psi}, \; mL - a \le x \le mL + a \quad (2.3a)$$

where

$$\psi = \pi x/L, \quad \psi_a = \pi a/L \quad (2.3b)$$

Averaging (2.3a) over one period gives the applied pressure as

$$\bar{p} = \frac{E^*L}{4\pi R}\sin^2\psi_a \quad (2.4)$$

The contact force per unit depth and per period (with unit N/m) is

$$P = \bar{p}L = \frac{E^*L^2}{4\pi R}\sin^2\psi_a \quad (2.5)$$

Due to the periodic symmetry, we only need to consider one period of the surface. Consider the central period ($m=0$), where the contact is symmetric with respect to the z-axis, and focus on the half period $0 \le x \le L/2$. The surface normal displacement is (Johnson, 1985):

$$u_z(x) = \frac{L^2}{4\pi^2 R}\cos(2\psi) + C, \;\; 0 \le x \le a \quad (2.6a)$$

$$u_z(x) = \frac{L^2}{4\pi^2 R}\left[\cos(2\psi) + 2\sin\psi\sqrt{\sin^2\psi - \sin^2\psi_a} - 2\sin^2\psi_a \ln\frac{\sin\psi + \sqrt{\sin^2\psi - \sin^2\psi_a}}{\sin\psi_a}\right] + C, \;\; a \le x \le \frac{L}{2} \quad (2.6b)$$

where C is a constant determined by the chosen datum for displacement. Consequently, the derivative of the surface normal displacement with respect to x are

$$\frac{\partial u_z}{\partial x} = -\frac{L}{2\pi R}\sin(2\psi), \;\; 0 \le x \le a \quad (2.7a)$$

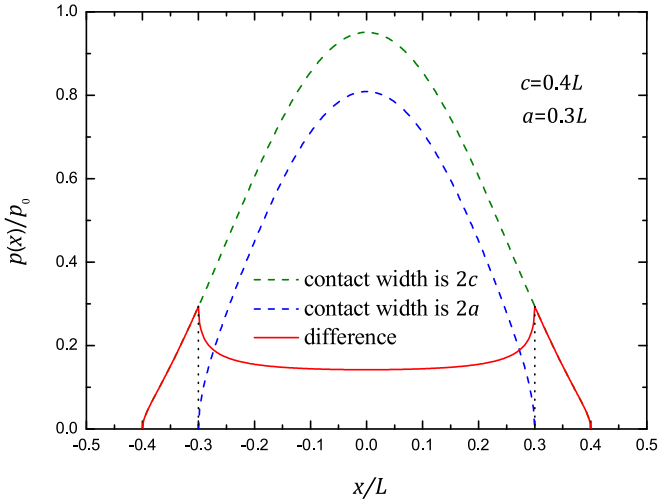

Fig. 3. The difference between two Westergaard solutions with contact half-width a and c for surface pressure within a period. Here, $p_0 = E^*L/2\pi R$.

$$\frac{\partial u_z}{\partial x} = -\frac{L}{2\pi R}\left[\sin(2\psi) - 2\cos\psi\sqrt{\sin^2\psi - \sin^2\psi_a}\right], \;\; a \le x \le \frac{L}{2} \quad (2.7b)$$

2.2. Double-Westergaard model

To account for adhesive interactions, the double-Hertz model of Greenwood and Johnson (1998) can be adopted for the present study following the basic idea of representing the adhesive tensile traction as the difference of two Hertz type pressure distributions. Here, the difference of two Westergaard pressure distribution functions with contact half-widths a and c can be found from Eq. (2.3) as

$$p(x) = \frac{E^*L}{2\pi R}\cos(\psi)\left[\sqrt{\sin^2\psi_c - \sin^2\psi} - \sqrt{\sin^2\psi_a - \sin^2\psi}\right], \quad 0 \le x \le a, \quad (2.8a)$$

$$p(x) = \frac{E^*L}{2\pi R}\cos\psi\sqrt{\sin^2\psi_c - \sin^2\psi}, \;\; a \le x \le c < \frac{L}{2} \quad (2.8b)$$

with the corresponding derivative of the surface normal displacement,

$$\frac{\partial u_z}{\partial x} = 0, \;\; 0 \le x \le a \quad (2.9a)$$

$$\frac{\partial u_z}{\partial x} = -\frac{L}{\pi R}\cos\psi\sqrt{\sin^2\psi - \sin^2\psi_a}, \;\; a \le x \le c < \frac{L}{2} \quad (2.9b)$$

where $\psi_c = \pi c/L$.

Defining $p_0 = E^*L/2\pi R$ as a reference pressure, Fig. 3 plots the distributions of the normalized pressures p/p_0 resulting from the difference between two Westergaard solutions with contact half-widths a and c, as shown in Eq. (2.8). It can be observed that the resulting pressure distribution steadily increases from the center of the contact region to a peak value at $x=a$ and then decreases to zero at $x=c$. In the following, the pressure in Eq. (2.8) scaled by an arbitrary factor $\lambda(>0)$ will be employed to model the adhesive tensile traction, resulting in the final distribution of surface traction when combined with an original Westergaard pressure. Under this treatment, the adhesive tensile traction for $0 \le x \le c$ can be

written as

$$p_A(x) = -\lambda \frac{E^* L}{2\pi R} \cos\psi \left[\sqrt{\sin^2\psi_c - \sin^2\psi} - \sqrt{\sin^2\psi_a - \sin^2\psi} \right] \quad 0 \le x \le a, \tag{2.10a}$$

$$p_A(x) = -\lambda \frac{E^* L}{2\pi R} \cos\psi \sqrt{\sin^2\psi_c - \sin^2\psi}, \quad a \le x \le c < \frac{L}{2} \tag{2.10b}$$

The maximum magnitude is

$$\sigma_0 = \lambda \frac{E^* L}{2\pi R} \cos\psi_a \sqrt{\sin^2\psi_c - \sin^2\psi_a} \tag{2.11}$$

Alternatively, the adhesive traction can be expressed in terms of σ_0 as

$$p_A(x) = -\sigma_0 \frac{\cos\psi \left[\sqrt{\sin^2\psi_c - \sin^2\psi} - \sqrt{\sin^2\psi_a - \sin^2\psi} \right]}{\cos\psi_a \sqrt{\sin^2\psi_c - \sin^2\psi_a}} \quad 0 \le x \le a\ , \tag{2.12a}$$

$$p_A(x) = -\sigma_0 \frac{\cos\psi}{\cos\psi_a} \frac{\sqrt{\sin^2\psi_c - \sin^2\psi}}{\sqrt{\sin^2\psi_c - \sin^2\psi_a}}, \quad a \le x \le c < \frac{L}{2} \tag{2.12b}$$

which corresponds to a normal force per period:

$$P = \frac{E^* L^2}{4\pi R} \left[\sin^2\psi_a - \lambda \left(\sin^2\psi_c - \sin^2\psi_a \right) \right] \tag{2.13}$$

The derivative of the surface normal displacement within the cohesive zone is

$$\frac{\partial u_z}{\partial x} = \frac{(1+\lambda)L}{\pi R} \cos\psi \sqrt{\sin^2\psi - \sin^2\psi_a} - \frac{L}{2\pi R} \sin(2\psi), \quad a \le x \le c < L/2\ , \tag{2.14}$$

and the resulting separation between the contact bodies is obtained from the geometric relation as

$$h = -\delta + f(x) + u_z, \quad a \le x \le c < L/2 \tag{2.15a}$$

and accordingly

$$\frac{\mathrm{d}h}{\mathrm{d}x} = \frac{(1+\lambda)L}{\pi R} \cos\psi \sqrt{\sin^2\psi - \sin^2\psi_a}, \quad a \le x \le c < \frac{L}{2} \tag{2.15b}$$

In Eq. (2.15a), δ denotes the indentation depth at the contact center and $f(x)$ has been defined in Eq. (2.1c). Recalling the boundary condition $h(a)=0$, the separation within the cohesive zone can be derived from Eq. (2.15b) as

$$h(x) = \frac{(1+\lambda)L^2}{2\pi^2 R} \sin\psi \left[\sqrt{\sin^2\psi - \sin^2\psi_a} - \sin\psi_a \ln \frac{\sin\psi + \sqrt{\sin^2\psi - \sin^2\psi_a}}{\sin\psi_a} \right] \quad a \le x \le c < L/2 \tag{2.16}$$

The adhesion energy is defined as the work needed to separate a unit area of two adhered surfaces to infinity. Since the separation vanishes for $0 \le x \le a$ and the traction vanishes for $c \le x \le L/2$ within each period, we have

$$\Delta\gamma = -\int_0^\infty p_A(h)\mathrm{d}h = -\int_a^c p_A(x)\frac{\mathrm{d}h}{\mathrm{d}x}\mathrm{d}x \tag{2.17}$$

Inserting Eqs. (2.10b) and (2.15b) into Eq. (2.17) leads to

$$\Delta\gamma = \lambda(1+\lambda)\frac{E^* L^2}{2\pi^2 R^2} I(a,c) \tag{2.18a}$$

where

$$I(a,c) = \int_a^c \cos^2\psi \sqrt{\sin^2\psi_c - \sin^2\psi} \sqrt{\sin^2\psi - \sin^2\psi_a}\mathrm{d}x \tag{2.18b}$$

To determine λ, a transition parameter is introduced as (Baney and Hui, 1997; Jin et al., 2014)

$$\mu = \frac{4}{\pi^{2/3}}\mu_T = 4\left(\frac{R\Delta\gamma^2}{\pi^2 E^{*2} z_0^3}\right)^{1/3} \approx 4\sigma_0\left(\frac{R}{\pi^2 E^{*2}\Delta\gamma}\right)^{1/3} \tag{2.19}$$

where μ_T denotes the classical Tabor parameter representing the ratio of the elastic displacement of the surfaces at pull-off to the effective range of surface forces characterized by z_0 (Tabor, 1977). Under this condition, a relationship between λ and μ can be established by combining Eqs. (2.11) and (2.19) as follows

$$\mu = 2\lambda \frac{L}{\pi} \cos\left(\frac{\pi a}{L}\right) \sqrt{\sin^2\left(\frac{\pi c}{L}\right) - \sin^2\left(\frac{\pi a}{L}\right)} \left(\frac{E^*}{\pi^2 R^2 \Delta\gamma}\right)^{1/3} \tag{2.20}$$

2.3. Non-dimensional results

The above results can be summarized in a dimensionless form. By introducing the following non-dimensional parameters:

$$a^* = \frac{a}{L}, \quad c^* = \frac{c}{L}, \quad P^* = \frac{4\pi RP}{E^* L^2}, \quad \alpha = 4\pi R\sqrt{\frac{2\Delta\gamma}{E^* L^3}} \tag{2.21}$$

the dimensionless normal load can be obtained from Eq. (2.13) as

$$P^* = \sin^2(\pi a^*) - \lambda\left[\sin^2(\pi c^*) - \sin^2(\pi a^*)\right] \tag{2.22}$$

and the relationship between a and c defined in Eq. (2.18) can be normalized as

$$1 = \lambda(1+\lambda)\frac{16}{\pi\alpha^2} I^* \tag{2.23a}$$

where

$$I^* = \int_A^C \sqrt{1-X^2}\sqrt{C^2-X^2}\sqrt{X^2-A^2}\mathrm{d}X \tag{2.23b}$$

with

$$A = \sin(\pi a^*), \quad C = \sin(\pi c^*) \tag{2.23c}$$

In Eq. (2.23a), λ is related to the transition parameter through

$$\mu = \frac{2\lambda}{\pi}\cos(\pi a^*)\sqrt{\sin^2(\pi c^*) - \sin^2(\pi a^*)}\left(\frac{\alpha^2}{32}\right)^{-1/3} \tag{2.24}$$

To eliminate λ, combining Eqs. (2.22), (2.23a) and (2.24) results in

$$P^* = A^2 - \frac{\Sigma_0}{2}\sqrt{\frac{C^2-A^2}{1-A^2}} \tag{2.25a}$$

$$1 = \frac{\Sigma_0}{2\sqrt{1-A^2}\sqrt{C^2-A^2}}\left(1 + \frac{\Sigma_0}{2\sqrt{1-A^2}\sqrt{C^2-A^2}}\right)\frac{16}{\pi\alpha^2} I^* \tag{2.25b}$$

where

$$\Sigma_0 = \pi\mu\left(\frac{\alpha^2}{32}\right)^{1/3} \tag{2.25c}$$

For comparison, the Westergaard (Johnson, 1985) and JKR types (Johnson, 1995) solutions for wavy contact are summarized as

$$P_W^* = \sin^2(\pi a^*), \quad P_{\mathrm{JKR}}^* = P_W^* - \alpha\sqrt{\tan(\pi a^*)} \tag{2.26a}$$

The corresponding Maugis–Dugdale solutions (Hui et al., 2001) for $a < c < L/2$ can be described in terms of the present notation as (Appendix A)

$$P^*_{\mathrm{MD}} = \sin^2(\pi a^*) - \Sigma_0\left[1 - \frac{2}{\pi}\arcsin\left(\frac{\cos(\pi c^*)}{\cos(\pi a^*)}\right)\right] \tag{2.27a}$$

with

$$\chi_1 \sin(\pi c^*) - P^*_{\mathrm{MD}}\chi_2 + \Sigma_0\Psi_c(c^*, a^*) = \frac{1}{\mu}\left(\frac{\alpha^4}{2}\right)^{1/3} \tag{2.27b}$$

where

$$\chi_1 = \sqrt{\sin^2(\pi c^*) - \sin^2(\pi a^*)},\quad \chi_2 = \ln\left[\frac{\sin(\pi c^*) + \chi_1}{\sin(\pi a^*)}\right] \tag{2.27c}$$

$$\Psi_c(c^*, a^*) = -\int_{a^*}^{c^*} \ln\left|\frac{\chi_3(c^*) + \chi_3(t)}{\chi_3(c^*) - \chi_3(t)}\right| \mathrm{d}t,\quad \chi_3(\eta) = \sqrt{1 - \frac{\sin^2(\pi a^*)}{\sin^2(\pi\eta)}} \tag{2.27d}$$

Based on Eq. (2.25a–c), Figs. 4a and b display the equilibrium $P^* - a^*$ curves with $a < c < L/2$ predicted by the present double-Westergaard (D-W) model under different values of μ for $\alpha = 0.3$ and $\alpha = 0.6$, respectively. The corresponding Westergaard, JKR and Maugis–Dugdale (M-D) types of solutions are also included for comparison. From this figure, both the D-W curve and the M-D curve are expected to approach the JKR curve as μ increases. Besides, it can be seen that both the D-W and M-D curves nearly agree with each other for smaller a^* but differ appreciably from each other for larger a^*. It is different from the case involving only a single cylindrical asperity where both D-W and M-D curves nearly coincide for the full range of a^* (Jin et al., 2014). This can be attributed to the effect of periodical boundary, which confines a^* and becomes evident as a^* approaches to the period boundary.

In order to compare the theoretical solutions of D-W and M-D models with the numerical results based on the Lennard–Jones (L-J) potential (Wu, 2012), the normalized half-width $b^*(=a^* + 0.4(c^* - a^*))$ is adopted according to Lantz et al., (1997) and Wu (2012). Fig. 5 shows the comparison of the $P^* - b^*$ curves of these three models for different values of α and μ. From this figure, it can be observed that the similar trend shared by the D-W and M-D curves almost agrees with that of L-J curves for small α and large μ, but differs appreciably from that of L-J curves for large α and small μ. This implies that the equilibrium state for $a < c < L/2$ is sensitive to the adhesive traction form when the effect of periodical boundary becomes evident. Compared with the M-D results, in fact, the present D-W curves seems to be more easily affected by the effect of periodical boundary, this is because the interaction zone of the D-W model is larger than that of M-D model for the same σ_0 and $\Delta\gamma$, and hence it saturates at a period more quickly with increasing load.

2.4. Special cases

The analysis thus far has implicitly assumed that the interaction zone is strictly confined within a single period, i.e., $c < L/2$, which need not always be the case. Solutions can also be obtained for $c = L/2$, corresponding to the limiting case with the adhesion force acting along the whole interface. Under this circumstance, the dimensionless normal load is given by

$$P^* = A^2 - \Sigma_0/2 \tag{2.28a}$$

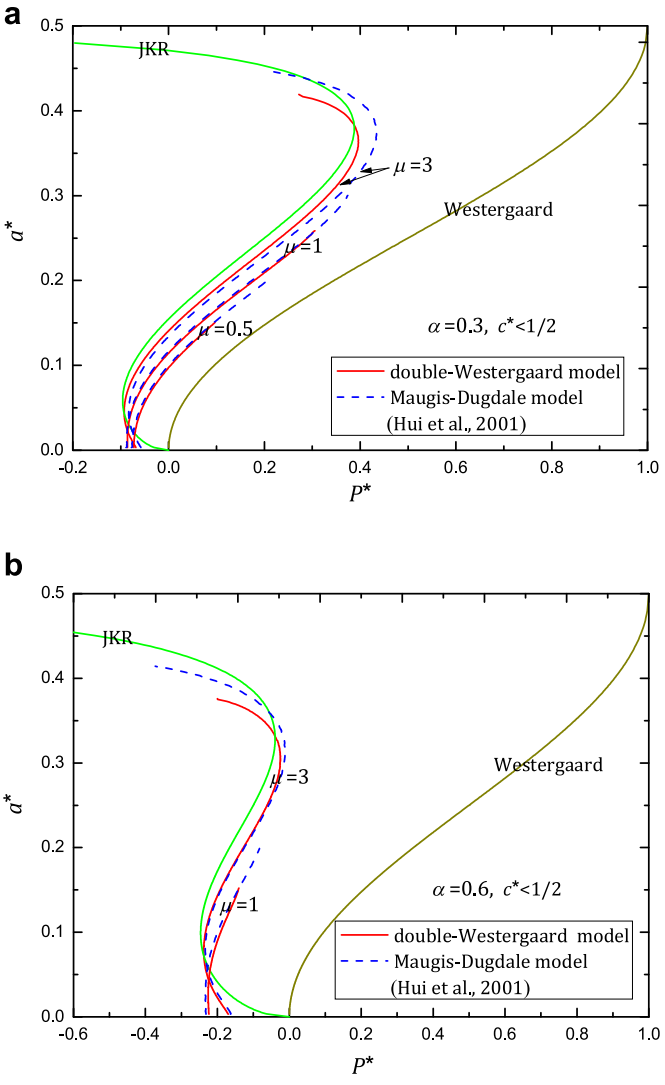

Fig. 4. The equilibrium $P^* - a^*$ curves with $a < c < L/2$ under different values of μ for (a) $\alpha = 0.3$ and (b) $\alpha = 0.6$. The corresponding Westergaard, JKR-type and Maugis–Dugdale solutions are also included for comparison.

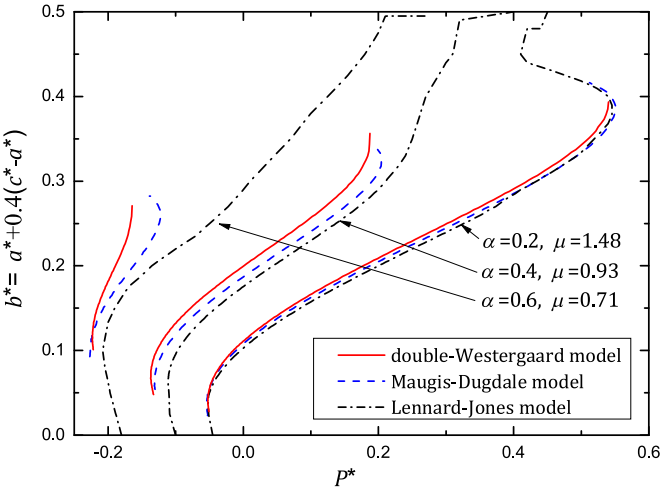

Fig. 5. Comparison of the $P^* - b^*$ curves predicted by the double-Westergaard, Maugis–Dugdale and Lennard–Jones models for different values of α and μ.

in which case the $c \sim a$ relationship (2.25b) is replaced by the following inequality constraint in terms of a,

$$\frac{\Sigma_0}{2\left(1-A^2\right)}\left[1+\frac{\Sigma_0}{2\left(1-A^2\right)}\right]\frac{16}{\pi\alpha^2}I_A^* - 1 < 0 \tag{2.28b}$$

where

$$I_A^* = \int_A^1 \left(1-X^2\right)\sqrt{X^2-A^2}\,dX \tag{2.28c}$$

Furthermore, full contact occurs ($a=c=L/2$) if the pressure exceeds the maximum value of the right hand side of Eq. (2.28a), i.e.,

$$P^* \geq 1 - \Sigma_0/2 \tag{2.29}$$

In summary, three different types of solutions are possible. In the first case, $c < L/2$ and there exists a gap region ($c < |x| < L/2$) without adhesive interactions. In the second case, $a < c = L/2$ and the adhesion force acts along the whole interface. The third case corresponds to full contact ($a=c=L/2$) between the wavy and flat surfaces. Up to this point, the main equations of the double-Westergaard model for wavy contact have been established.

3. Reduction

According to the classical cohesive zone models of axisymmetric spheres (Maugis, 1992; Greenwood and Johnson, 1998) and of two-dimensional cylinders (Johnson and Greenwood, 2008; Jin et al., 2014), a large cohesive zone holds for small and rigid solids with a small Tabor number, while a small cohesive zone applies to relatively large and soft bodies corresponding to a large Tabor parameter. This also holds true for the wavy contact case, where the transition parameter μ defined in Eq. (2.19) is similar to the Tabor parameter. Both Westergaard and JKR types of solutions can be recovered from the present double-Westergaard model by taking opposite limiting values of μ.

3.1. Westergaard limit

Since both the contact region and interaction zone are confined within a single period, a large cohesive zone corresponds to small a with $c=L/2$. For a smaller transition parameter μ ($\mu \ll 1$), $\Sigma_0 \to 0$ and Eq. (2.28a) becomes

$$P^* = \sin^2(\pi a^*) \tag{3.1}$$

which coincides perfectly with the Westergaard solution (Westergaard, 1939). Under this condition, the inequality constraint of a^* in Eq. (2.28b) is automatically satisfied.

3.2. JKR-type limit

For a small cohesive zone ($c \to a$) with a large transition parameter μ ($\mu \gg 1$), the factor λ becomes large ($\lambda \gg 1$) as suggested by Eq. (2.20). Under this circumstance, the applied load in Eq. (2.22) and the $c \sim a$ relation in Eq. (2.23a) reduce to

$$P^* = \sin^2(\pi a^*) - 2\lambda \sin(\pi a^*)[\sin(\pi c^*) - \sin(\pi a^*)] \tag{3.2a}$$

$$1 = \lambda^2 \frac{16}{\pi\alpha^2} I_0^* \tag{3.2b}$$

with

$$I_0^* = \lim_{C\to A}\int_A^C \sqrt{1-X^2}\sqrt{C^2-X^2}\sqrt{X^2-A^2}\,dX$$

$$= 2A\sqrt{1-A^2}\int_A^C \sqrt{C-X}\sqrt{X-A}\,dX$$

$$= \frac{\pi}{4}\sin(\pi a^*)\cos(\pi a^*)[\sin(\pi c^*) - \sin(\pi a^*)]^2 \tag{3.2c}$$

Inserting Eq. (3.2c) back into Eq. (3.2b) yields

$$\lambda[\sin(\pi c^*) - \sin(\pi a^*)] = \frac{\alpha}{2\sqrt{\sin(\pi a^*)\cos(\pi a^*)}} \tag{3.3}$$

Substituting Eq. (3.3) into (3.2a) leads to

$$P^* = \sin^2(\pi a^*) - \alpha\sqrt{\tan(\pi a^*)} \tag{3.4}$$

which is precisely the JKR solution for wavy contact (Johnson, 1995).

Under this circumstance, the state of full contact ($a=c=L/2$) is achieved when $P^* \to -\infty$, as indicated by Eq. (2.29). This singularity in the equilibrium curve is attributed to the assumption that a perfect joint exhibits the theoretical strength of the interface (Johnson, 1995).

4. Results and discussions

4.1. Loading/unloading curves

Different values of the non-dimensional parameter α defined in Eq. (2.21) lead to different adhesive contact behaviors during loading and unloading. As pointed by Johnson (1995), α^2 represents the ratio of the surface energy in one wavelength to the elastic strain energy when the wavy surface is flattened. Figs. 6–8 plot the half-widths of contact and interaction zones versus the applied load per period for small, moderate and large values of α (0.3, 0.6 and 1), respectively.

Fig. 6a–e correspond to $\alpha=0.3$ with various values of μ. We first discuss the case in Fig. 6b with $\mu=1$. At zero load, adhesion causes the surfaces to jump into contact with a finite value of contact half-width (A→B), which is found by the intersection of a vertical line at $P^*=0$ with the red solid line. The corresponding values of c^* versus load are shown by the black solid line. In the loading stag, a^* increases until full contact (B→D), while c^* increases to 1/2 and then remains constant. Full contact persists under further load increase. During the unloading stage, full contact continues until point D, a further decrease in load causes a^* to decrease following the path D→B. Then a tensile load is needed to separate the adhered surfaces with a^* shrinking to zero (B→E). At the point B the loading and unloading stages begin to differ, giving rise to a hysteresis loop whose area quantifies the energy loss during the deformation process. As μ becomes small enough (e.g. $\mu=0.1$), as shown in Fig. 6a, the equilibrium P^*-a^* curve prevails only for $c^*=1/2$ and approaches the Westergaard solution with reduced hysteresis loop. When μ becomes large enough, e.g. $\mu=5$, as shown in Fig. 6e, the equilibrium P^*-a^* curve nearly prevails for $c^* < 1/2$ and approaches the JKR solution. Larger hysteresis loop arises due to additional jump instabilities, including a sudden jump into full contact (snapping contact) (C→D) and a sudden jump completely out of contact (snapping detachment) (F→G). Note that if the contact bodies are unloaded from a point between points B and C, then pull-off occurs at the lower inflection point of the red solid curve. These two opposite limits have been examined in Section 3.

The behaviors exhibited in Figs. 6c and d are similar to Fig. 6b except for more jump instabilities and larger hysteresis loop. For $\mu=2.5$ in Fig. 6c, jump instabilities are observed during both loading and unloading stages between the red solid line ($a^* < c^* < 1/2$) and the red dash-dot line ($a^* < c^*=1/2$), labeled by C→D and F→G, respectively. For $\mu=3$ in Fig. 6d, full contact is achieved

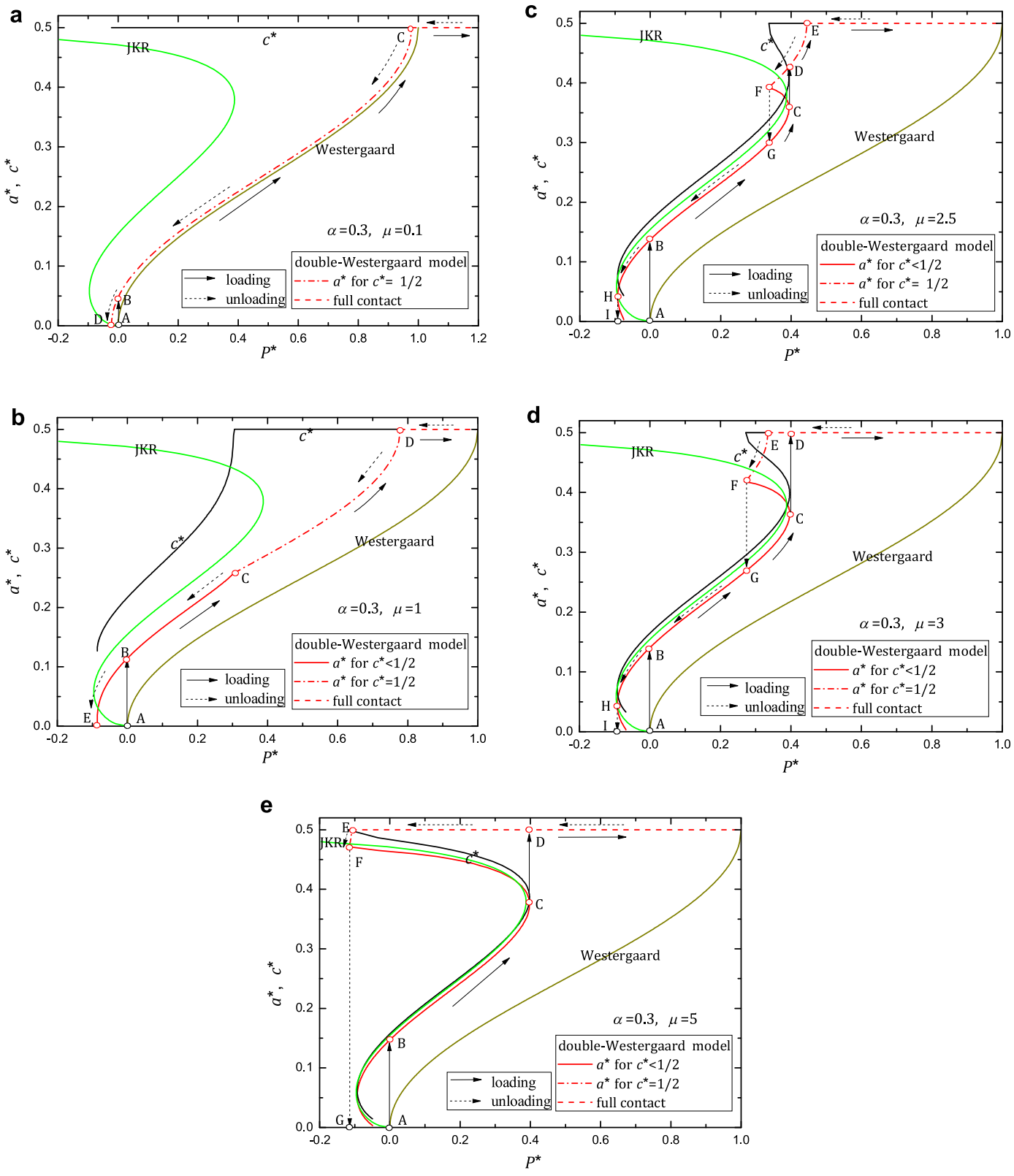

Fig. 6. The half-widths of contact and interaction zones versus the normal load with $\alpha = 0.3$ for (a) $\mu = 0.1$, (b) $\mu = 1$, (c) $\mu = 2.5$, (d) $\mu = 3$ and (e) $\mu = 5$.

upon an immediate jump from the red solid line. As seen from both Fig. 5c and d, separation occurs at a critical tensile force corresponding to a jump out of contact, i.e., the pull-off force per period (H→I). Note that the red solid curves have unstable regions in most cases, this is due to loading/unloading stages are both under a load controlled mode. Under this condition, the portions of the curve with a positive slope allow stable attachment/detachment, whereas the portions with a negative slop are unstable.

For a moderate value of α, e.g., $\alpha = 0.6$, Fig. 7a–e correspond to Fig. 6a–e with the same value of μ, respectively. This implies that the wavy surface becomes smoother with increasing α with fixed μ. It can be seen that the red dash-dot line ($a^* < c^* = 1/2$)

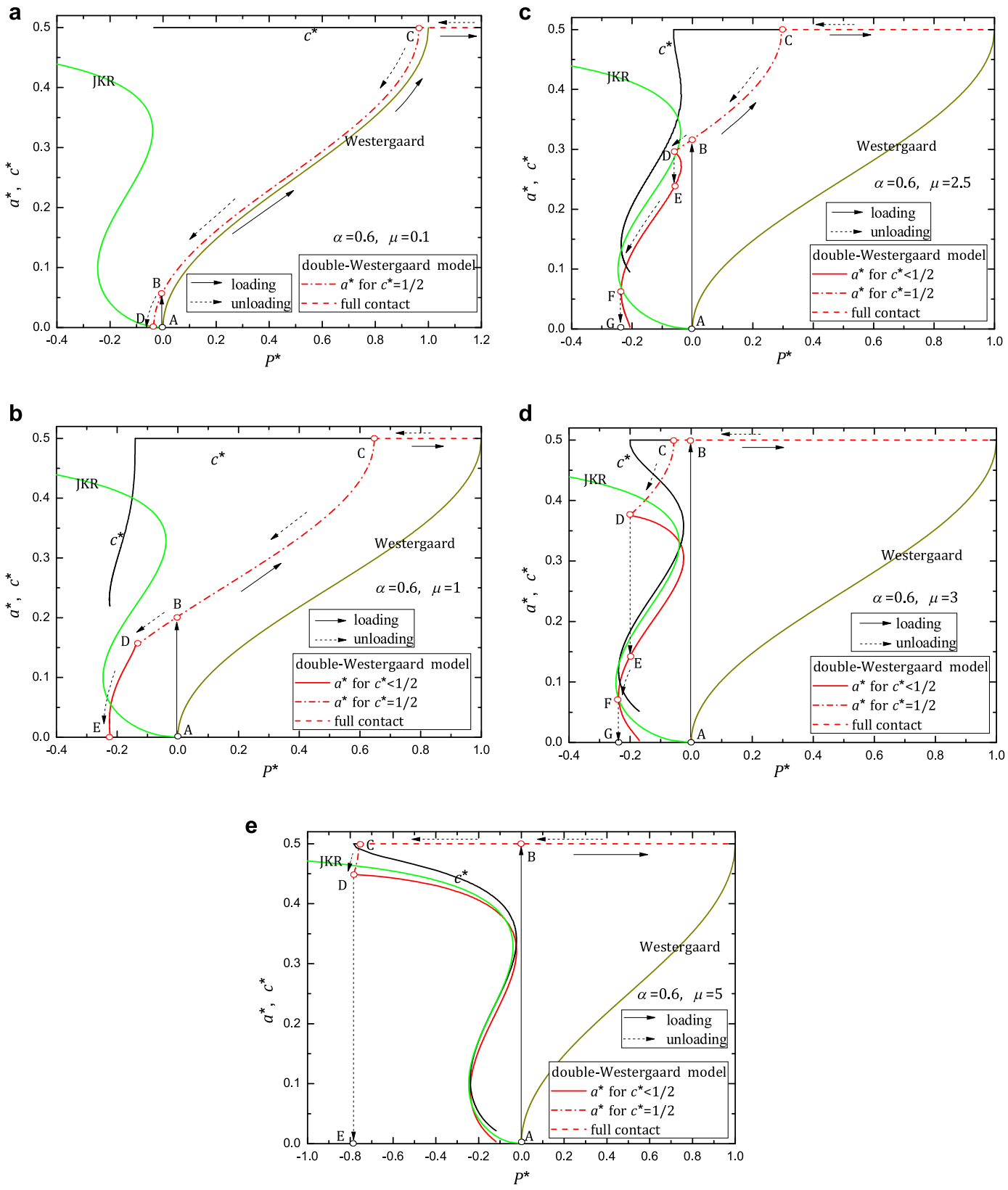

Fig. 7. The half-widths of contact and interaction zones versus the normal load with $\alpha = 0.6$ for (a) $\mu = 0.1$, (b) $\mu = 1$, (c) $\mu = 2.5$, (d) $\mu = 3$ and (e) $\mu = 5$.

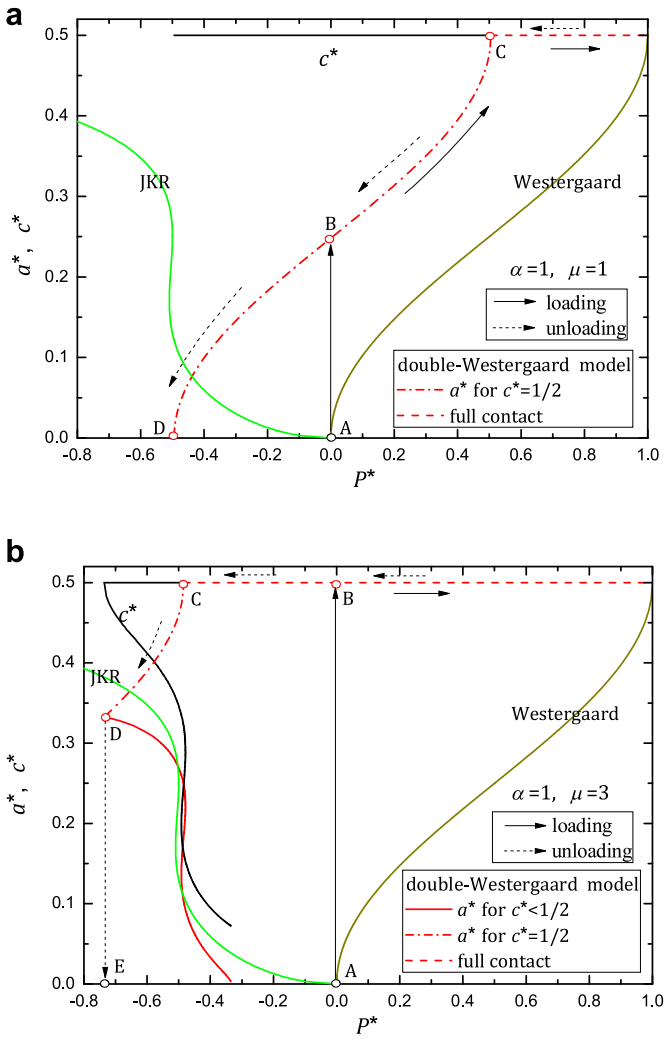

Fig. 8. The half-widths of contact and interaction zones versus the normal load with $\alpha=0.6$ for (a) $\mu=0.1$ and (b) $\mu=1$.

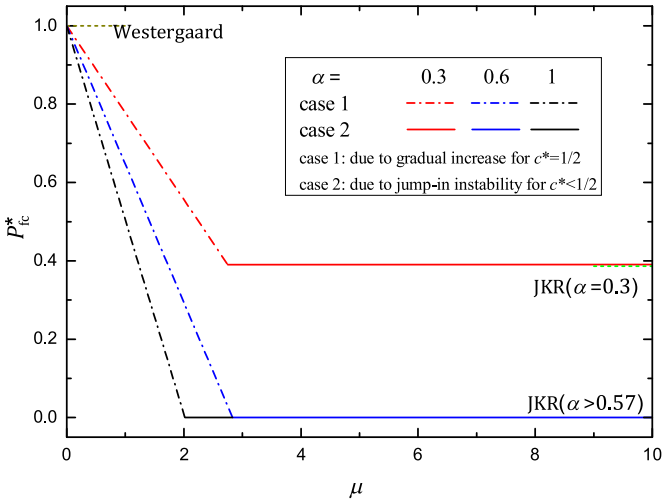

Fig. 9. Critical compressive force within a period to achieve full contact as a function of the transition parameter for different values of α.

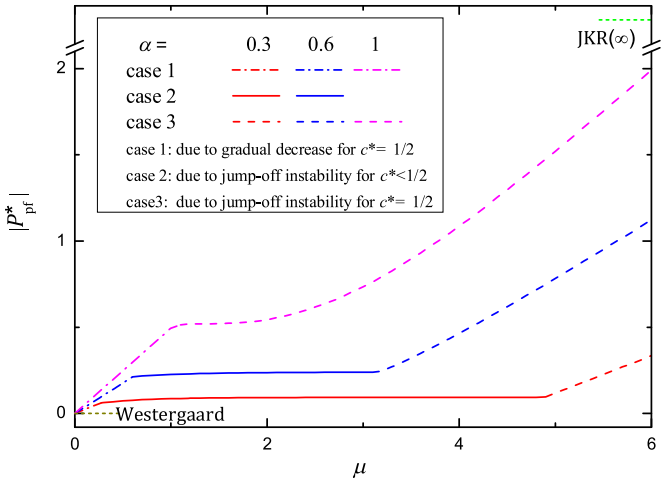

Fig. 10. Pull-off force within a period as a function of the transition parameter for different values of α.

tends to be more pronounced than that in Figs 6a-e. Interestingly, snapping adhesive contact occurs at a greater value of a^* and even full contact is available in the absence of an applied load for larger values of μ, as shown in Figs. 7d-e.

For a large value of α, e.g., $\alpha=1$, Fig. 8a and b show two typical behaviors with $\mu=1$ and $\mu=3$, respectively. As expected, the red dash-dot line ($a^* < c^*=1/2$) prevails over the whole range for $\mu=1$, whereas jump-off instabilities occurs immediately from the red dash-dot line for $\mu=3$. Moreover, hysteresis loop becomes more pronounced with greater resulting energy loss compared with the cases of lower α with the same μ. This implies decreasing waviness size by decreasing both the amplitude and period with a fixed curvature can induce more energy loss due to adhesion hysteresis.

From the above figures, different transition processes between partial and full contact involving jump instabilities can be observed during loading/unloading, which was also demonstrated in the theoretical study based on the Maugis–Dugdale model (Adams, 2004) and the numerical simulation based on the Lennard–Jones potential (Wu, 2012). These adhesive behaviors depend on both material properties and surface topography through two non-dimensional parameters α and μ. In the contact experiment between a rippled surface and a rigid spherical indenter, Jin et al. (2011) also found different transition modes from partial to full contact on samples with different waviness-amplitudes but the same wavelength.

4.2. Critical forces

As a measure of the interfacial strength of a wavy surface, it is helpful to examine the critical compressive force for full contact and the critical pull-off force for detachment (pull-off force), which can be identified from the P^*-a^* curves shown in Figs. 6–8.

Fig. 9 plots the normalized critical compressive force P^*_{fc} within a period to achieve full contact versus the transition parameter α. It can be seen that P^*_{fc} initially decreases from the Westergaard value at $\mu=0$ and finally attains the JKR value at a finite μ. The dash-dot lines correspond to the case when the contact size gradually increases to fill out the whole period resulting in full contact, whilst the solid lines correspond to the case when full contact occurs due to a jump-in instability. It is noted that the JKR value for $\alpha < 0.57$ depends on the value of α and vanishes for $\alpha > 0.57$ (Hui et al., 2001).

The variation of the normalized pull-off force P^*_{pf} within a period as a function of the transition parameter is shown in Fig. 10. It can be observed that the magnitude of P^*_{pf} initially increases from the Westergaard value at $\mu=0$ and finally approaches the JKR value with increasing μ. The dash-dot lines correspond to the case when the contact size gradually shrinks to zero, whilst the solid

and dash lines correspond to the case when detachment occurs due to pull-off instability for $c^* < 1/2$ and $c^* = 1/2$, respectively. The pull-off force predicted by the Westergaard model vanishes in the absence of adhesion, but becomes infinity in the JKR model due to an assumption of the interface theoretical strength (Johnson, 1995). For a prescribed value of μ, in addition, larger α leads to greater magnitude of the pull-off force. This implies that decreasing waviness size by decreasing both the amplitude and period with a fixed curvature can cause interface strengthening.

A common feature of Figs. 9 and 10 is that a transition from the Westergaard to JKR values is captured with increasing μ. As two opposite limiting cases, the Westergaard and JKR models for wavy contact are unified in the present double-Westergaard model.

5. Conclusions

The plane strain adhesive contact between a wavy surface and a flat surface has been investigated by extending the classical double-Westergaard model of Greenwood and Johnson (1998). This is achieved by expressing the adhesive force in terms of the difference between two Westergaard pressure distribution functions with different contact widths. When the interaction zone is less than a period, closed-form analytical solutions are obtained for the interfacial traction, deformation and equilibrium relation among applied load, contact half-width and cohesive zone size within a period. When the adhesion force acts throughout the whole period, two additional solutions have also been constructed.

Based on the present results, a complete transition between the Westergaard and JKR-type contact models is captured by defining a dimensionless transition parameter, which governs the range of applicability of different models. Westergaard and JKR-type solutions are included as two limiting cases of the present model. Loading and unloading behaviors are characterized by one or more jumps among three different equilibrium states. Depending on two non-dimensional parameters α and μ, different transition processes between partial and full contact are identified during loading and unloading. Decreasing waviness size by decreasing both the amplitude and period with a fixed curvature are found to enhance adhesion both by increasing the magnitude of pull-off force and through more energy loss due to adhesion hysteresis.

Acknowledgments

The authors gratefully acknowledge support from the National Natural Science Foundation (11402247, 91216201), Foundation of President of The China Academy of Engineering Physics (CAEP) (201402073), Program for Changjiang Scholars, the key subject "Computational Solid Mechanics" of CAEP, and the Focused Science and Technology Development Fundation of CAEP (2014A0203006).

Appendix A: Maugis–Dugdale solution for adhesive contact of a wavy surface

For $a < c < L/2$, according to Hui et al. (2001), the normalized force predicted by the Maugis–Dugdale model of a wavy surface is

$$P^*_{\mathrm{MD}} = \sin^2(\pi a^*) - \Sigma_0\left[1 - \frac{2}{\pi}\arcsin\left(\frac{\cos(\pi c^*)}{\cos(\pi a^*)}\right)\right] \tag{A1}$$

where P^*, a^* and c^* are defined in Eq. (2.21). Furthermore, c^* is related to a^* through

$$\sin^2(\pi c^*) + \Psi_{\mathrm{JKR}}(P^*, c^*, a^*) + \Sigma_0\Psi_c(c^*, a^*) = \Delta_{\mathrm{cod}} \tag{A2}$$

where

$$\Psi_{\mathrm{JKR}}(P^*, c^*, a^*) = -\sin^2(\pi c^*) + \chi_1 \sin(\pi c^*) - \chi_2 P^*_{\mathrm{MD}} \tag{A3}$$

$$\Psi_c(c^*, a^*) = -\int_{a^*}^{c^*} \ln\left|\frac{\chi_3(c^*) + \chi_3(t)}{\chi_3(c^*) - \chi_3(t)}\right| \mathrm{d}t, \quad \Delta_{\mathrm{cod}} = \frac{2\pi^2 R\Delta\gamma}{L^2\sigma_0} \tag{A4}$$

$$\chi_1 = \sqrt{\sin^2(\pi c^*) - \sin^2(\pi a^*)}, \quad \chi_2 = \ln\left[\frac{\sin(\pi c^*) + \chi_1}{\sin(\pi a^*)}\right] \tag{A5}$$

$$\chi_3(\eta) = \sqrt{1 - \frac{\sin^2(\pi a^*)}{\sin^2(\pi\eta)}} \tag{A6}$$

In fact, Δ_{cod} can be rewritten in terms of the transition parameter μ in Eq. (2.19) and the non-dimensional parameter α in Eq. (2.21) as

$$\Delta_{\mathrm{cod}} = \frac{1}{\mu}\left(\frac{\alpha^4}{2}\right)^{1/3} \tag{A7}$$

Inserting Eqs. (A3) and (A7) back into Eq. (A2) yields

$$\chi_1 \sin(\pi c^*) - P^*_{\mathrm{MD}}\chi_2 + \Sigma_0\Psi_c(c^*, a^*) = \frac{1}{\mu}\left(\frac{\alpha^4}{2}\right)^{1/3} \tag{A8}$$

References

Adams, G.G., 2004. Adhesion at the wavy contact interface between two elastic bodies. J. Appl. Mech. 71, 851–856.
Baney, J.M., Hui, C.Y., 1997. A cohesive zone model for the adhesion of cylinders. J. Adhesion Sci. Technol. 11, 393–406.
Block, J.M., Keer, L.M., 2008. Periodic contact problems in plane elasticity. J. Mech. Mater. Struct. 3, 1207–1237.
Briggs, G.A.D., Briscoe, B.J., 1977. The effect of surface topography on the adhesion of elastic solids. J. Phys. D Appl. Phys. 10, 2453–2466.
Carbone, G., Mangialardi, L., 2004. Adhesion and friction of an elastic half-space in contact with a slightly wavy rigid surface. J. Mech. Phys. Solids 52, 1267–1287.
Chumak, K., 2016. Adhesive contact between solids with periodically grooved surfaces. Int. J. Solids Struct. 78-79, 70–76.
Etsion, I., 2005. State of the art in laser surface texturing. ASME J. Tribol. 127, 248–253.
Etsion, I., Halperin, G., 2002. A laser surface textured hydrostatic mechanical seal. Tribol. Trans. 45, 430–434.
Fuller, K.N.G., Roberts, A.D., 1981. Rubber rolling on rough surfaces. J. Phys. D 14, 100–104.
Fuller, K.N.G., Tabor, D., 1975. The effect of surface roughness on adhesion of elastic solids. Proc. R. Soc. Lond. A 345, 327–342.
Greenwood, J.A., Johnson, K.L., 1998. An alternative to the Maugis model of adhesion between elastic spheres. J. Phys. D 31, 3279–3290.
Guduru, P.R., 2007. Detachment of a rigid solid from an elastic wavy surface: theory. J. Mech. Phys. Solids 55, 445–472.
Haiat, G., Huy, M.C.P., Barthel, E., 2003. The adhesive contact of viscoelastic spheres. J. Mech. Phys. Solids 51, 69–99.
Hui, C.Y., Glassmaker, N.J., Tang, T., Jagota, A., 2004. Design of biomimetic fibrillar interfaces: 2. Mechanics of enhanced adhesion. J. R. Soc. Lond. Interface 1, 35–48.
Hui, C.Y., Lin, Y.Y., Baney, J.M., Kramer, E.J., 2001. The mechanics of contact and adhesion of periodically rough surface. J. Polym. Sci. Part B 39, 1195–1214.
Jin, C., Khare, K., Vajpayee, S., Yang, S., Jagota, A., Hui, C.Y., 2011. Adhesive contact between a rippled elastic surface and a rigid spherical indenter: from partial to full contact. Soft Matter 7, 10728–10736.
Jin, F., Guo, X., 2013. Mechanics of axisymmetric adhesive contact of rough surfaces involving power-law graded materials. Int. J. Solids Struct. 50, 3375–3386.
Jin, F., Guo, X., Gao, H., 2013. Adhesive contact on power-law graded elastic solids: the JKR-DMT transition using a double-Hertz model. J. Mech. Phys. Solids 61, 2473–2492.
Jin, F., Zhang, W., Guo, X., Zhang, S., 2014. Adhesion between elastic cylinders based on the double-Hertz model. Int. J. Solids Struct. 51, 2706–2712.
Jin, F., Zhang, W., Wan, Q., Guo, X., 2016. Adhesive contact of a power-law graded elastic half-space with a randomly rough rigid surface. Int. J. Solids Struct. 81, 244–249.
Johnson, K.L., 1985. Contact Mechanics. Cambridge University Press, Cambridge.
Johnson, K.L., 1995. The adhesion of two elastic bodies with slightly wavy surfaces. Int. J. Solids Struct. 32, 423–430.
Johnson, K.L., Greenwood, J.A., 2008. A Maugis analysis of adhesive line contact. J. Phys. D 41, 155315–1-6.
Kesari, H., Lew, A., 2011. Effective macroscopic adhesive contact behavior induced by small surface roughness. J. Mech. Phys. Solids 59, 2488–2510.
Kim, H.C., Russell, T.P., 2001. Contact of elastic solids with rough surfaces. J. Polym. Sci., Part B, Polym. Phys. 39, 1848–1854.
Komvopoulos, K., 2003. Adhesion and friction forces in microelectromechanical systems: mechanisms, measurement, surface modification techniques, and adhesion theory. J. Adhesion Sci. Technol. 17, 477–517.

Lantz, M.A., O'Shea, S.J., Welland, M.E., Johnson, K.L., 1997. Atomic-force-microscope study of contact area and friction on $NbSe_2$. Phys. Rev. B 55, 10776–10785.
Maugis, D., 1992. Adhesion of spheres: the JKR-DMT transition using a Dugdale model. J. Colloid Interface Sci. 150, 243–269.
Morrow, C., Lovell, M.R., Ning, X., 2003. A JKR-DMT transition solution for adhesive rough surface contact. J. Phy. D Appl. Phys. 36, 534–540.
Santos, R., Gorb, S., Jamar, V., Flammang, P., 2005. Adhesion of echinoderm tube feet to rough surfaces. J. Exp. Biol. 208, 2555–2567.
Tabor, D., 1977. Surface forces and surface interactions. J. Colloid Interf. Sci. 58, 2–13.
Wei, Z., He, M., Zhao, Y.P., 2010. The effects of roughness on adhesion hysteresis. J. Adhesion Sci. Tech. 24, 1045–1054.
Westergaard, H.M., 1939. Bearing pressures and cracks. J. Appl. Mech. 6 A49–A53.
Wu, J.J., 2012. Numerical simulation of the adhesive contact between a slightly wavy surface and a half-Space. J. Adhesion. Sci. Technol. 26, 331–351.
Zhang, W., Jin, F., Guo, X., Zhang, S., 2014. Adhesive contact on randomly rough surfaces based on the double-Hertz model. J. Appl. Mech. 81, 051008.
Zilberman, S., Persson, B.N.J., 2002. Adhesion between elastic bodies with rough surfaces. Solid State Commun 123, 173–177.